Microstructural evolution and mechanical behaviour of alkali activated fly ash binder treated clay

Elodie Coudert, Dimitri Deneele, Giacomo Russo, Enza Vitale, Alessandro Tarantino

MICROSTRUCTURAL EVOLUTION AND MECHANICAL BEHAVIOUR OF ALKALI ACTIVATED FLY ASH BINDER TREATED CLAY

Elodie Coudert[a,b], Dimitri Deneele[c,d], Giacomo Russo[e*], Enza Vitale[e], Alessandro Tarantino[b]

[a] Department of Civil and Mechanical Engineering, University of Cassino and Southern Lazio, Via Gaetano di Biasio, 43, 03043 Cassino, FR, Italy

[b] Department of Civil and Environmental Engineering, University of Strathclyde, 75 Montrose Street, Glasgow, Scotland, G1 1XJ, United Kingdom

[c] Institut des Matériaux Jean Rouxel (IMN), Université de Nantes, CNRS, 2 rue de la Houssinière, BP 32229, 44322 Nantes Cedex 3, France

[d] GERS-LEE, Univ Gustave Eiffel, IFSTTAR, F-44344 Bouguenais, France

[e] Department of Earth Science, Environment and Resources, University of Napoli Federico II, Via Cinthia 21 80126, Napoli, Italy

* Corresponding Author, giarusso@unina.it

Author Accepted Manuscript
Construction and Building Materials, 285(2021), Elsevier
DOI: 10.1016/j.conbuildmat.2021.122917

Abstract

This work focuses on the use of alkali activated fly ash-based binder to enhance engineering characteristics of soft clay-rich soils and as a substitute to standard stabilisers (e.g., lime or cement). Especially, it examines the microstructural evolution of a calcium-rich fly ash from coal combustion-based binder activated by a sodium-based alkaline solution. To this end, the processes generating the microstructure and the evolution of the pore network over time are investigated. A second point addressed by this study is how the presence of kaolin particles affects the microstructural features of the binder. The microstructure has therefore been investigated by considering the binder alone and the binder mixed with kaolin. The effects of microstructural evolution have been observed at macroscopic level by means of one-dimensional compression tests.

The combination of completing techniques has been used including Optical microscopy, Scanning Electron Microscopy and Mercury Intrusion Porosimetry in order to gain an overview of the complex pore structure.

Microstructural changes occur around calcium-containing phases derived from fly ash which are the reactive phases of the system. Namely, the dissolution of calcium-rich grains leads to the formation of new compounds that first cover the grain surfaces and then further grow into the available space. Furthermore, the evolution of the pore network over time is characterized by a progressive filling of capillary pores by new compounds while small nanometric pores are being formed and associated with the newly formed silicate-calcium chains. Similar tendencies are observed when the binder is mixed with the soil although the general porosity is lesser due to the filling of pores by small-sized kaolinite platelets. Experimental evidences at microscale level have been linked to the macroscopic behaviour of treated soil.

Keywords: Kaolin, Fly ash, Soil treatment, Alkali activated material, Microstructure, Mechanical Behaviour

1. Introduction

Soft clay-rich soils are frequently encountered in construction sites. Their poor mechanical performances represent a critical issue in engineering projects and are

49 commonly improved by using either Ordinary Portland Cement or lime as a soil stabiliser.
50 Nevertheless, those conventional stabilisers are associated with high carbon dioxide
51 emissions and energy intensive processes, significantly increasing the worldwide carbon
52 footprint (Scrivener and Kirkpatrick, 2008, Xi et al. 2016). The anthropogenic carbon
53 emissions have been increasingly recognized to be one of the main responsible of climate
54 changes and environmental degradation (United Nations, 2004). In the low carbon
55 agenda, it is then of outmost relevance the development of cost- and carbon-efficient
56 technologies. In the construction sector, for which cement production contributes to at
57 least 5–8% of global carbon dioxide emissions (Scrivener and Kirkpatrick, 2008),
58 alternative industrial by-products (e.g. high-calcium fly ash, rice husk ash, silica fume)
59 have been successfully used as cementing agents in soil improvement resulting in
60 environmental and economic benefits (Basha et al. 2003, Nalbantoğlu 2004, Sargent
61 2015, James & Pandian 2016).
62 As an alternative, the use of Alkali Activated Material (AAM) as a soil stabiliser is
63 gaining more and more attention over the past ten years. Alkali Activated Materials are
64 defined as any binder system derived by the reaction of an alkali metal source (usually
65 alkali hydroxide and alkali silicate solutions) with a solid aluminosilicate powder
66 (commonly metakaolin, fly ash, blast furnace slag or natural pozzolan) (Buchwald et al.,
67 2003; Shi et al., 2006). It gives a hardened material at room temperature with mechanical
68 properties potentially suitable for Portland cement replacement. Alkali Activated
69 Materials could constitute a viable sustainable soil binder because of their lower CO_2
70 emission process compared to traditional Portland cement (Duxson et al. 2007; McLellan
71 et al. 2011, Zhang et al. 2014). Furthermore, recent studies have shown a positive
72 potential and feasibility results of using alkali activated binders for soil improvement, and

this not only for different types of soil i.e. clayey soil (Wilkinson et al., 2010; Singhi et al., 2016; Vitale et al. 2017, Vitale et al. 2019; Vitale et al. 2020a, 2020b), sandy clay (Cristelo et al., 2011), marl, marlstone (Cristelo et al., 2012), silty sand (Rios et al., 2016) or else road aggregates (Tenn et al., 2015); but also for different applications i.e. in deep soft soil (Cristelo et al., 2011), at shallow depth (Zhang et al., 2013) or in rammed earth construction (Silva et al., 2013).

Works on alkali activated binder treated soils are relatively recent and constitute a novel domain of application. Our study particularly focuses on the use of a calcium-rich fly ash from coal combustion activated by sodium-based alkaline solution as a binder for clay kaolin stabilisation. Kaolin was selected as a model soil that represent a wide class of clays encountered in engineering projects and for maintaining the system simple. Kaolinite being not reactive to alkaline activation at ambient temperature, a more reactive aluminosilicate source is required for chemical reactions to occur. For that purpose, a calcium-rich fly ash was selected in the context of resource-saving being an industrial waste. The main aim is to assess the feasibility of using this novel binder for soil treatment.

When addressing the feasibility of using a class of material for a novel application, there are several important parameters to consider such as the composition, microstructure and processing which all ultimately affect the performance-to-cost ratio of a material (Askeland et al., 2011). A detailed understanding of both the composition but also the structure of the binder across length scales is therefore required in order to control materials properties through its processing.

Two main length scales of investigation can be distinguished with relevant importance. A first one is the particle scale and corresponds to the identification of the different phases

97 constituting particles in terms of chemical composition and crystal structure. Important
98 properties of particles depend on the arrangements of atoms and types of bonding within
99 each phase (Clemens et al., 2008). A second scale of observation is at the level of group
100 of particles, or microstructure. Microstructural investigations for alkali activated
101 materials are of prime importance as their physical properties depend largely on their pore
102 network characteristics and microstructure (Nath et al., 2016; Lawrence and Jiang, 2017).
103 This is associated with the fact that the microstructure controls the transport properties of
104 the binder and the stability of the matrix when exposed to aggressive agents (van Deventer
105 et al., 2015).
106 In our previous study the physicochemical evolution of similar systems than those herein
107 studied was carried out i.e. identification and evolution of the constitutive phases until 28
108 days of curing time at an atomic level. It showed that the soil i.e. kaolin was not reactive.
109 Whereas, fly ash was partly reactive. Some of its phases such as the vitreous phase and
110 quartz were mainly unreactive, while calcium-containing phases represented the reactive
111 phases. The new compounds formed were an amorphous silicate consisting of chains
112 combined with calcium probably incorporating three-dimensional four-fold aluminium
113 environments and thenardite Na_2SO_4 (Coudert et al., 2019).
114 The present work focusses on the microstructural description, taking into account the
115 knowledge gained about the physicochemical evolution of the system. The study was
116 designed in three stages. An initial stage consisted in the identification of the phases
117 present in the reactive aluminosilicate source i.e. the original calcium-rich fly ash and
118 description of their structure, shape and size distribution. The different constituents of fly
119 ash being inhomogeneously reactive (Provis and Deventer, 2009), it was important to
120 identify the reactive phases around which microstructural changes were predominant. A

second stage focussed on the investigation of the microstructural evolution of the alkali activated fly ash binder during the first 28 days of curing, including (i) a description of the dispersion and arrangement of phases, (ii) an understanding of which processes generate the microstructure over time and (iii) a pore network characterisation. Fly ash being a highly inhomogeneous material (Provis and Deventer, 2009), a key point was to determine the homogeneity of processes across the sample at a microscopic level. Besides, a particular emphasis was put at understanding microstructural changes and processes around calcium particles which are the main reactive phases. A third stage focussed on the interaction of the fly ash-based binder with the kaolin clay to understand how the presence of kaolin modifies the microstructural features of the system. As previously stated, kaolinite is unreactive during the alkaline activation. However, because of its small size kaolinite acts as a filler of the porosity (Coudert et al., 2019) and undoubtedly plays a role on the microstructural evolution. The effects at macroscopic level have been highlighted with reference to one dimensional compression results, showing the improvement of the mechanical performances of the treated soil as function of binder percentage and curing time. A final comparison between the performance of cement treated soil with alkali activated binder treated soil has shown for highlighting the effectiveness of the improvement.

2. Material and methods

2.1 Materials

A Polish fly ash derived from hard coal and coal slime combustion in fluidised bed boiler was used. Its chemical analysis is given in Table 1, and consists primarily of SiO_2, Al_2O_3

and CaO. The fly ash contains, approximately, 52% of particles sized lower than 45 µm and 41% lower than 10 µm.

Speswhite kaolin provided by Imerys Minerals UK, and whose chemical composition is given in Table 1 was used. It is mainly constituted of kaolinite (95%) and secondarily of muscovite (4%) (Chemeda, 2015). The kaolin contains, approximately, 100 % of particles sized lower than 10 µm and 80 % lower than 2 µm.

A unique alkaline solution was used: a sodium silicate with a mass ratio SiO_2/Na_2O of 1.7 and a dry mass percentage of 44%; supplied by Woellner Group and named GEOSIL 34417.

Table 1 - Chemical composition (wt. %) of raw fly ash and kaolin.

	SiO_2	Al_2O_3	Fe_2O_3	CaO	CaO_{free}[a]	MgO	SO_3	Na_2O	K_2O	H_2O	L.o.I.
Fly ash	39.4	19.8	7.4	18.6	5.2	1.8	4.1	2.0	1.8	0.0	1.7[b]
Kaolin	49.2	34.5	1.2	0.0	0.0	0.2	0.0	0.1	1.7	13.1	12.0[c]

[a] Free calcium oxide content
[b] L.o.I = Loss on ignition 900 °C
[c] L.o.I = Loss on ignition 1000 °C

2.2 Sample preparation

Sample preparation consisted in (i) mix of liquid sources i.e. silicate and water (ii) mix of aluminosilicate powders i.e. fly ash and kaolin in the case of soil-source sample (iii) mix of (i) and (ii) previously prepared.

For microstructural analyses, two types of mixes were studied and named F100 and KF50. F100 is the fly ash-based alkali activated binder. It corresponds to a solid phase made of fly ash only, whereas KF50 is the alkali activated binder treated soils and corresponds to a solid phase made of 50% of fly ash and 50% of kaolin in mass.

168 To ensure a good workability, the amount of added water with respect to the solid mass
169 (e.g. mass of kaolin and fly ash) was fixed to 50% for all the samples. Additionally, the
170 mass ratio of alkaline solution to fly ash was fixed to 50% for all the samples, giving the
171 initial molar ratios (considering that kaolin is unreactive): Si/Al = 2.0, Si/Na = 3.5 and
172 Al/Na = 1.8. The Al/Na ratio was not fixed to one because of the presence of calcium
173 ions in high quantity in our system playing a role of charge compensation as well as
174 sodium.
175 The paste obtained was poured in closed plastic molds and cured at room temperature (20
176 °C). Samples were finally demoulded and freeze-dried at curing times of 24 hours, 3, 7
177 or 28 days.
178 Samples for one dimensional compression tests were prepared with the described
179 technique. Three mixes have been considered in the study, namely KF10, KF20 and KF40
180 corresponding to a solid phase made of 10%, 20% and 40% of fly ash with reference to
181 dry mass of solids (fly ash+ kaolin). Remoulded samples were prepared by hand mixing
182 solids, alkaline solution and water at their liquid limits (i.e. w_L=67% for KF10, w_L=60%
183 for KF20, w_L=55% for KF40). Samples were poured in the mould and placed in
184 oedometer cell without compaction. Treated samples were cured for 24 hours, 7, 14, 28
185 and 60 days before mechanical testing.
186
187 *2.3 Methods*
188 Samples were studied by Optical and Scanning Electron Microscope from polished
189 section. Freeze-dried samples were impregnated under a vacuum with an acrylic resin
190 (LR White). The polymerisation of the resin was performed in an oven at 60 °C over 48
191 h. The samples were then polished with diamond powder. The observations from Optical

192 Microscopy were done with a Nikon LV100 polarizing optical microscope combined with
193 a ccd Nikon DS-2Mv camera and the NIS Element BS software. Whereas the
194 observations from Scanning Electron Microscope were done with a HITACHI SU5000
195 scanning electron microscope equipped with an energy-dispersive X-ray analyser
196 (Quantax microanalyser system composed of X-Flash® SDD detector and the Esprit
197 software). The polished samples were coated with carbon before the observation. The
198 microscope was operated at an accelerating voltage of 20 kV and working distances of
199 10 mm.
200 MIP tests were performed by a double chamber Micromeritics Autopore III apparatus. In
201 the filling apparatus (dilatometer) samples were outgassed under vacuum and then filled
202 by mercury allowing increase of absolute pressure up to ambient one. Using the same unit
203 the intrusion pressure was than raised up to approximately 200 kPa by means of
204 compressed air. The detected entrance pore diameters ranges between 134 μm and 7.3
205 μm (approximately 0.01 MPa - 0.2 MPa for a mercury contact angle of 139°). After
206 depressurisation to ambient pressure, samples were transferred to high-pressure unit,
207 where mercury pressure was increased up to 205 MPa following a previously set intrusion
208 program. The smallest detected entrance pore diameter was about 7 nm. Corrections to
209 pore-size distribution due to compressibility of intrusion system were applied performing
210 a blank test.
211 One dimensional compression tests have been performed in standard oedometer cells,
212 where vertical stress was conventionally applied in successive steps ($\Delta\sigma v/\sigma v = 1$) within
213 the stress interval $10 \div 2400$ kPa. Micrometer dial gauges with an accuracy of 0.001 mm
214 have been used to measure vertical displacements.
215

3. Results and discussion

The first section of results presents the general characteristics of the raw fly ash which constitutes the reactive aluminosilicate source of the mixes. The second part examines the microstructural evolution of the binder. The third part focusses on the description of system made by kaolin and the alkali activated binder and its mechanical performance.

3.1 Raw fly ash

The fly ash used here contains various components. Its composition consisting of (i) a vitreous phase and (ii) various crystalline phases i.e. calcium-containing minerals: anhydrite $CaSO_4$, calcite $CaCO_3$ and portlandite $Ca(OH)_2$, and other minerals: quartz SiO_2, feldspar $(K,Na,Ca)(Si,Al)_4O_8$, hematite Fe_2O_3 and muscovite $(Si_3Al)O_{10}(Al_2)(OH)_2K$ (Coudert et al., 2019).

Its particle size distribution reflects this diversity with 52 % of particles lower than 45 µm, 41 % of particles lower than 10 µm and 12 % of particles lower than 2 µm.

Figure 1 confirms this great variety also detectable by Scanning Electron Microscopy. In fact, the fly ash presents an extremely heterogeneous microstructure with particles of different shapes and ranging from 1 µm to more than 200 µm. The vitreous phase is itself heterogeneous and made of (i) some spherical particles (see G Figure 1B), (ii) bigger unshaped particles (see G Figure 1C) and (iii) aggregates of small particles primarily (see G Figure 1D).

Some crystallised angular shaped minerals can also be distinguished and correspond to quartz (see Q Figure 1A&D) or feldspar (see F Figure 1B).

Finally, regarding calcium-rich phases, our previous study showed that calcium-containing minerals i.e. anhydrite $CaSO_4$, calcite $CaCO_3$ and portlandite $Ca(OH)_2$ are

interlaced together (Coudert et al., 2019). Especially, they are interlinked within a nodule shape structure generally of 50 to 200 µm size as seen on Figure 1B (particle labelled C).

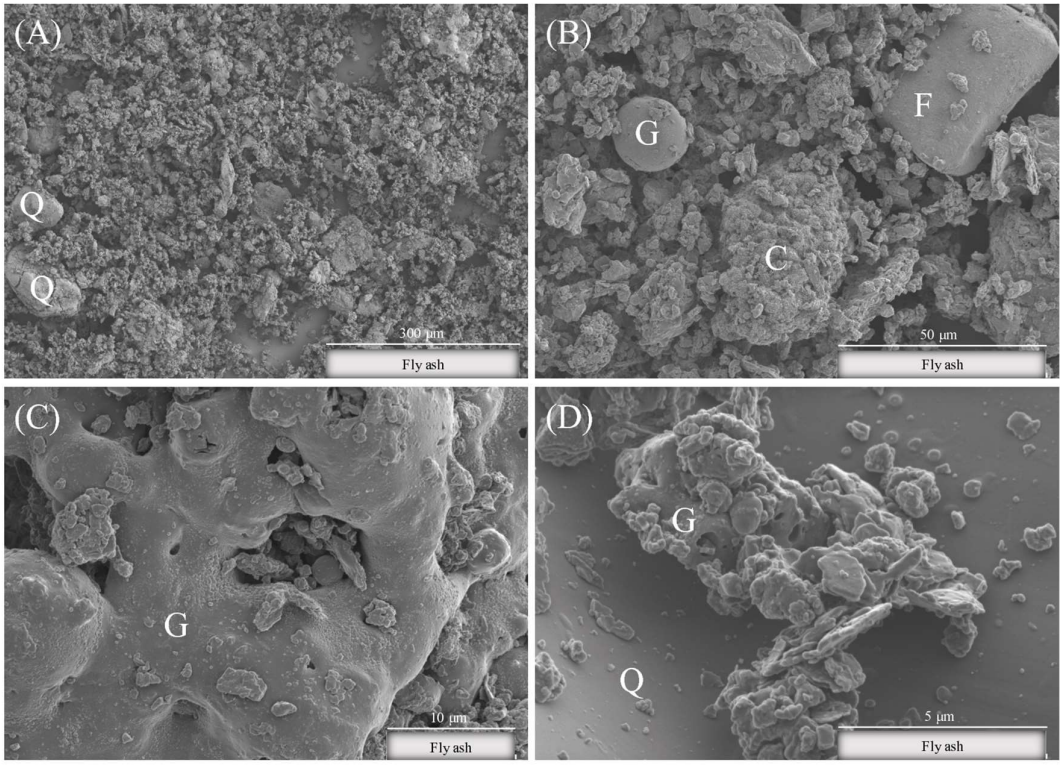

Fig. 1 SEM micrographs of the raw fly ash; C=calcium-rich particle; F=feldspar; G=glass; Q=quartz.

3.2 Alkali activated fly ash binder

3.2.1 Optical Microscopy

Figure 2 shows the microstructural evolution of the alkali activated fly ash binder over time by optical microscopy. Observations were carried out until 28 days as chemical reactions are fully developed at that curing time (Coudert et al., 2019).

After 24 hours of curing, dispersed dark spots of around 50 µm to 200 µm size are seen across the overall sample (see particles labelled C on Figure 2A&B), and correspond to reactive calcium-rich nodules by analogy with the previous observations of the raw fly

ash constituents (section 3.1). They represent approximatively 15 % of the mixture. Whereas the brown matrix includes the vitreous phase and calcium-free minerals from fly ash.

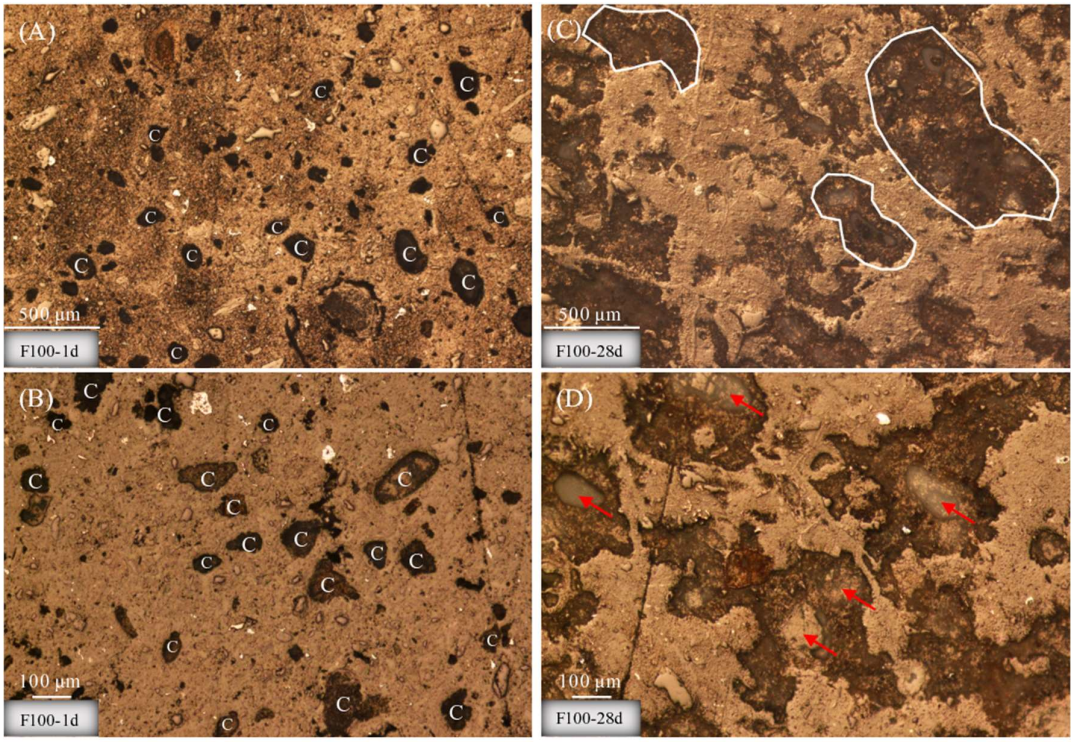

Fig. 2 Optical microscopy images of the alkali activated fly ash binder F100 (A) and (B) after 24 hours, (C) and (D) at 28 days; C=calcium-rich particle.

By comparison, at 28 days, no dark spots are visible but instead large dark zones whose edges are less well defined (see encircled areas on Figure 2C), and correspond to new products formed. Figure 2D shows a closer observation of those large dark reactive areas. The initial nodule shapes can still be distinguished at 28 days but instead of a dark spot as observed at 24 hours it is a hollowed greyish structure that is seen as shown by the red arrow (Figure 2D). This structure is associated with dissolution features over time of the calcium-rich phase, and in accordance with the previous results about the physicochemical evolution which indicate that calcium-containing phases are the main

reactive phases. New compounds corresponding to dark areas are therefore formed around the hollowed dissolved calcium nodules. Those new compounds have been identified in a previous study as thenardite Na_2SO_4, and an amorphous silicate consisting of chains combined with calcium probably incorporating three-dimensional four-fold aluminium environments (Coudert et al., 2019).

As a consequence of those observations, the spreading of the darker areas at 28 days gives an idea of the extent of the reaction and widening of the new compounds formation across samples. In this system, half of the sample encompasses the new compounds and is hence reactive whereas the initial calcium nodules represented only 15 % of the sample. Besides, those new compounds seem homogeneously spread across the sample which likely could give a homogeneously reinforced material at the macroscopic scale.

Results from optical microscopy therefore match with the observed physicochemical evolution i.e. principal changes occur around calcium-rich reactive particles. That is why the next session focusses on the in-situ microstructural transformation of calcium-rich phases induced by the alkaline solution.

3.2.2 Scanning Electron Microscopy (SEM)

Figure 3 shows microstructural observations from a polished section and combined chemical mappings of the alkali activated fly ash binder after 24 hours of curing. Chemical mappings on Figure 3B&C indicate the presence of a calcium-rich nodule labelled 1 on Figure 3A and predominantly made of calcium and sulphur. Additionally, those calcium-rich particles display a granular aspect on their surface.

Surrounding this calcium-rich particle, the area labelled 2 on Figure 3A corresponds to a porous zone distinguishable by the presence of dense black areas characteristic of the

294 filling resin of low atomic mass. Chemical mappings of that porous zone show an
295 enrichment in silicon and sodium (Figure 3D&E) indicating the presence of the sodium-
296 silicate Na_2SiO_3 alkaline solution at that short curing time. Additionally, filament like
297 structures are observed within that area (see red arrow on Figure 3A), and considered as
298 the beginning of the secondary phases formation i.e. the amorphous silicate consisting of
299 chains combined with calcium and potentially aluminium. In fact, a former study about
300 cementitious microstructures has shown the formation of similar arrangements associated
301 with Calcium Silicate Hydrates whose structure strongly resembles the one of our newly
302 formed chains (Scrivener, 2004). Moreover, it appears that those filament structures are
303 stacked around particles corresponding to the initiation of the reaction process after 24
304 hours of curing.
305 Figure 4 also shows microstructural observations of the alkali activated fly ash binder
306 after 24 hours of curing, and particularly illustrates the microstructural difference
307 between a calcium-rich particle and a particle from the vitreous phase both originally
308 present in the fly ash. They can both be distinguished by SEM by their chemical
309 composition and microstructural features. Regarding calcium-rich particles, they present
310 a nodule shape with a granular surface (see 3 on Figure 4A) as previously observed
311 (Figure 3A). Whereas particles from the vitreous phase display a vesicular structure (see
312 1 on Figure 4A) and can be distinguished using chemical mappings by their enrichment
313 in silicon and aluminium (Figure 4D&E).
314 In between those two particles, a porous area labelled 2 on Figure 4A and with filament
315 like structures can once again be observed and evidences the initiation of the reaction
316 processes. Consequently, from Figure 3 as from Figure 4 it is noticeable that the alkali
317 activated binder after 24 hours of curing presents a high porosity created by the fly ash

grains of various sizes and that is filled by water, alkaline solution, and the new product starting to be formed.

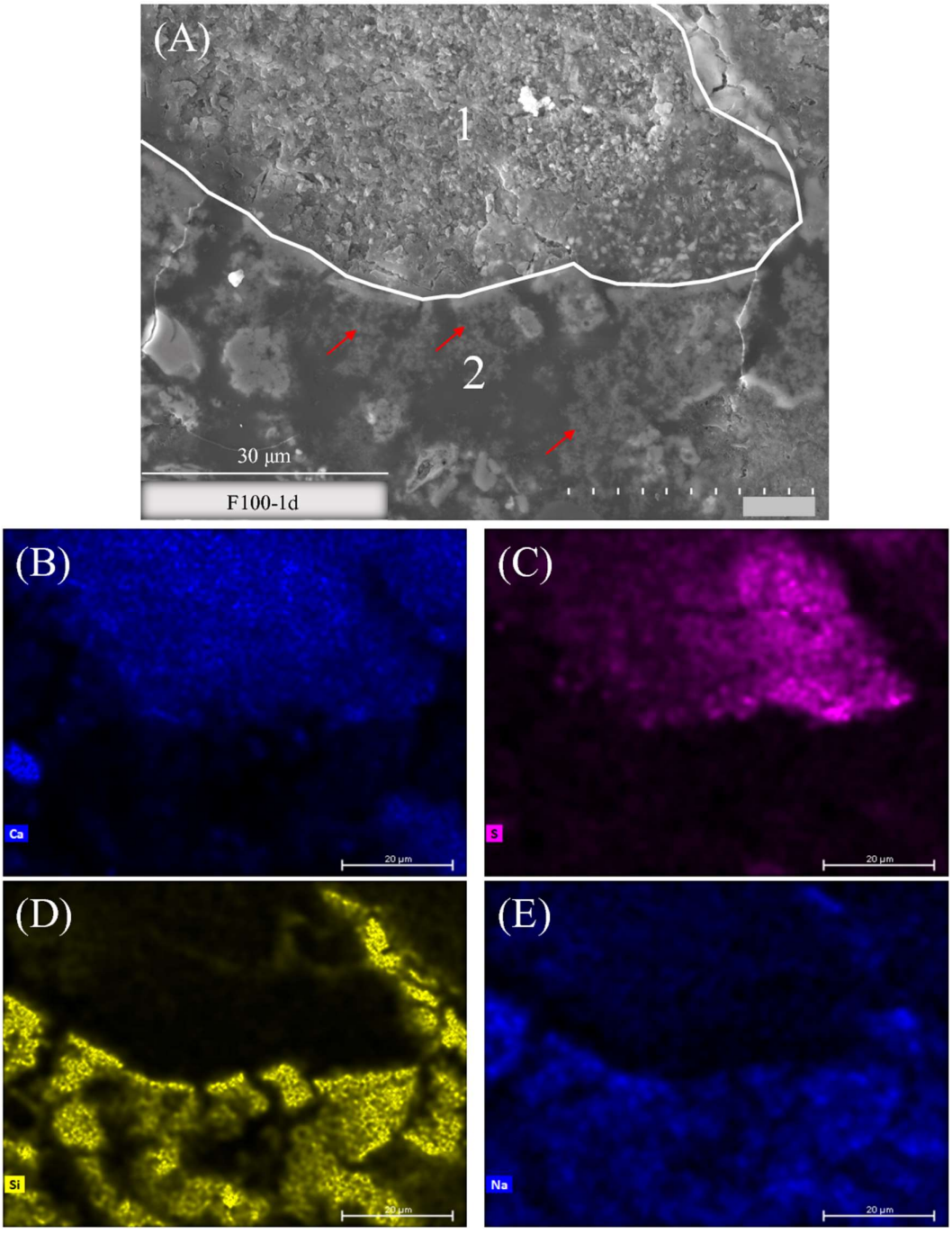

Fig. 3 SEM observations of the alkali activated fly ash binder F100 after 24 hours of curing: (A) SEM micrograph, and chemical mappings of: (B) calcium, (C) sulphur, (D) silicon and (E) sodium.

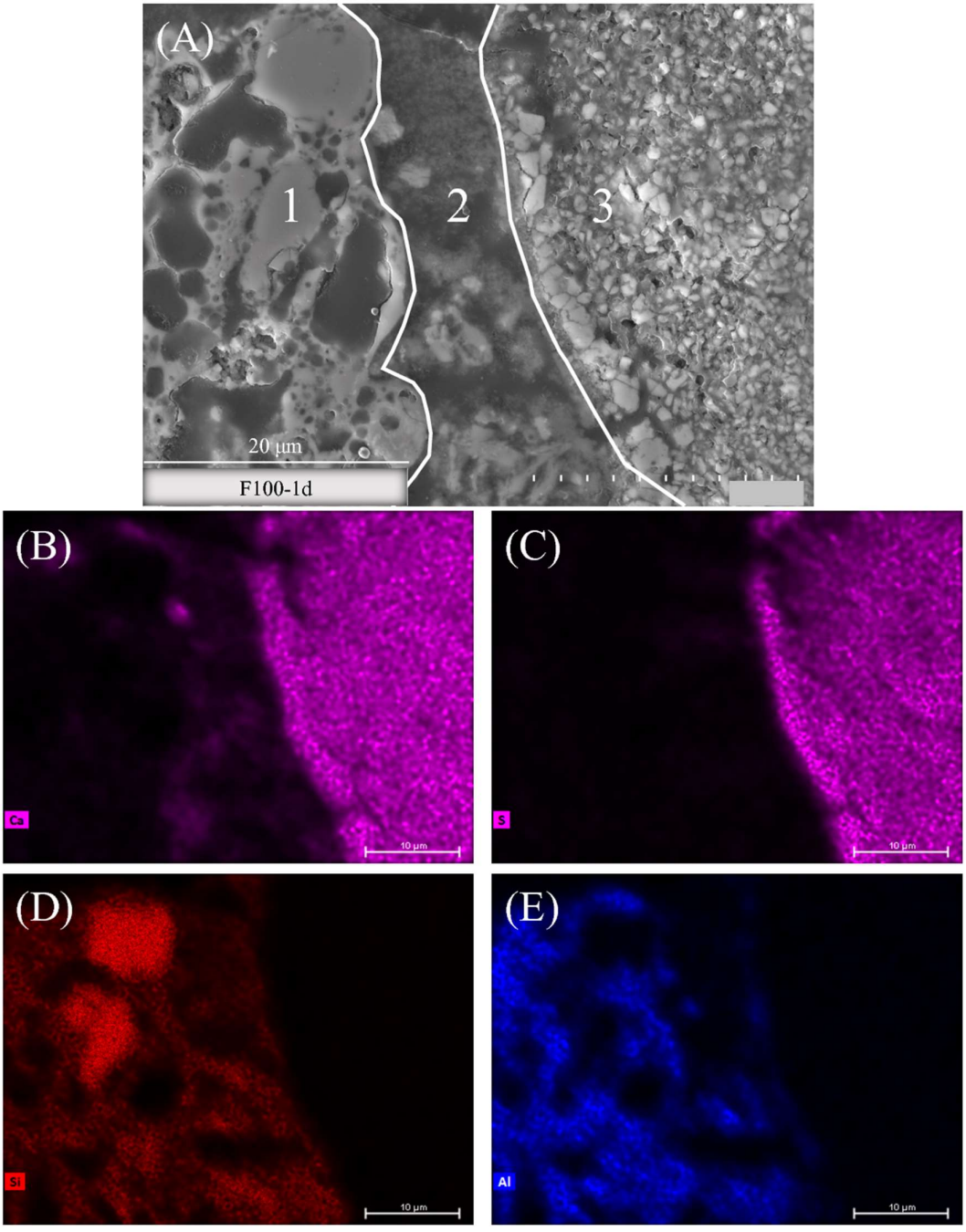

Fig. 4 SEM observations of the alkali activated fly ash binder F100 after 24 hours of curing: (A) SEM micrograph, and chemical mappings of: (B) calcium, (C) sulphur, (D) silicon and (E) aluminium

330

331 Figure 5 shows SEM observations and combined chemical mappings of the alkali
332 activated fly ash binder after 28 days of curing. It especially focuses on the interface
333 between a calcium-rich nodule labelled 1 and the surrounding matrix labelled 2.
334 Regarding the calcium-rich nodule, it displays a hollowed structure, especially in its
335 centre, and as similarly observed previously by optical microscopy in section 3.2.1. In
336 addition, those hollowed structures show dense black zones indicating the presence of
337 filling resin and therefore porosity. Those structural characteristics strongly contrast with
338 calcium nodules after 24 hours presenting a granular surface, and are attributed to the
339 dissolution of calcium-rich phases over time leaving behind a porous body. It is supported
340 by chemical mappings on Figure 5B&C showing a strong impoverishment in calcium and
341 sulphur in the hollowed area with respect to nodules after 24 hours.
342 An enrichment in calcium and sulphur is seen in the outer part of the nodule suggesting
343 a mechanism of dissolution of calcium and sulphur moving from the calcium nodules to
344 the matrix. Moreover, few silicon supplied in that system by the alkaline solution is
345 detected above the edges of the calcium nodule and inside implying that the alkaline
346 solution penetrates through the calcium-nodule accelerating its dissolution. The
347 coloration due to the silicon presence inside the nodule is few marked as unreactive quartz
348 which corresponds to intensely coloured and well defined edges spots on the silicon
349 chemical mapping (Figure 5D) are present in the matrix and induces a rescaling of the
350 silicon coloration.
351

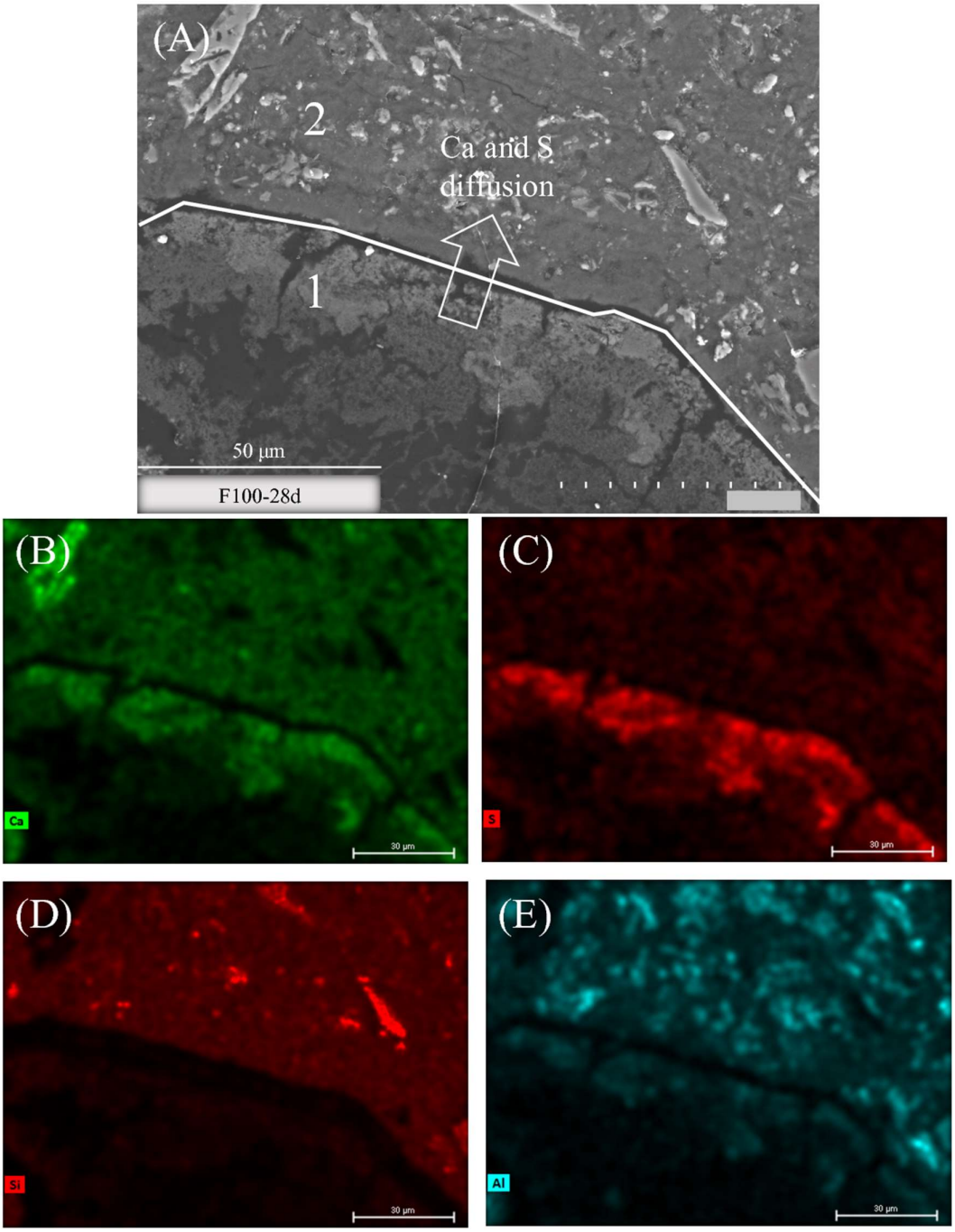

Fig. 5 SEM observations of the alkali activated fly ash binder F100 at 28 days: (A) SEM micrograph, and chemical mappings of: (B) calcium, (C) sulphur, (D) silicon and (E) aluminium.

Regarding the area surrounding the calcium nodule labelled 1, it is massive and presents a low porosity compared to the binder after 24 hours. It corresponds to the area where

359 new products are formed. Its chemical mappings show a high content of calcium and
360 silicon which is in accordance with the physicochemical investigation that showed the
361 formation of silicate chains combined with calcium over time. The wide diffusion of
362 calcium into the matrix is clearly seen from Figure 5 when compared to the binder after
363 24 hours of curing for which calcium is contained and restrained to the nodule surface
364 (see Figure 3 and Figure 4). Concerning sulphur elements, as well initially present in the
365 nodule in the form of anhydrite $CaSO_4$, its dissolution occurs in a lesser extent and seems
366 stopped to the outer part of the nodule at 28 days (Figure 5C). The physicochemical
367 evolution of this system showed that dissolved sulphur combine with sodium to form
368 thenardite Na_2SO_4 at 28 days (Coudert et al., 2019). Consequently, the presence of
369 thenardite is restrained to small areas around the calcium-rich particles, whereas silicate
370 two-dimensional chains combined with calcium are widely spread all around the calcium
371 nodules. The formation of this thenardite crust limited around calcium nodules can be
372 explained by the low amount of sulphur elements compared to calcium (see chemical
373 composition of the raw fly ash in Table 1), that already all precipitated in this small area.
374 The conjoint chemical mapping of sodium to localise thenardite is not shown here as
375 sodium is a volatile element for which it is difficult to get a chemical mapping showing
376 a reliable representativeness of sodium dispersion.
377 Finally, important crackings are observed around calcium-rich particle as seen on Figure
378 5 and are associated with shrinkage processes frequently observed for alkali activated
379 materials (Fang et al., 2018).
380

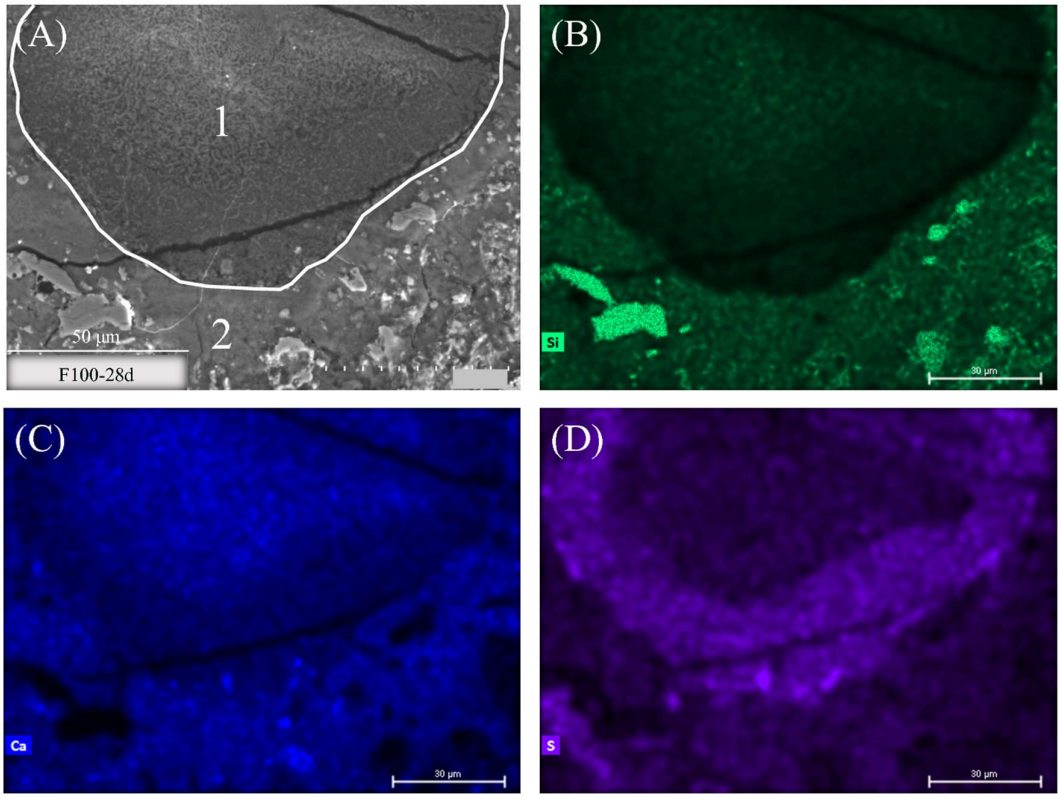

Fig. 6 SEM observations of the alkali activated fly ash binder F100 at 28 days: (A) SEM micrograph, and chemical mappings of: (B) silicon, (C) calcium and (D) sulphur.

Figure 6 shows the alkali activated fly ash binder at 28 days, and more particularly a calcium-rich reactive nodule labelled 1 surrounded by a dense matrix comprising both new products and non-reactive phases such as quartz or aluminium containing minerals. However, in that case the extent of dissolution of the calcium nodule appears lower as the hollowed structure is not seen but rather a granular microstructure similar of those observed after 24 hours. Chemical mappings show that the dissolution of that nodule did start as calcium is widely diffused into the matrix, and an enrichment in sulphur is once again seen in the outer part of the nodule. Nevertheless, the dissolution is at a different stage as calcium is still strongly detected in the centre of the nodule and no hollowed structure is noticed. Consequently, the extent of reaction of a calcium-rich nodule varies

locally. A lesser porosity of the calcium nodule could for instance moderates its dissolution. Its size, its content in calcium and sulphur or else the amount of water locally available are also all parameters that may locally affect the extent of reaction.

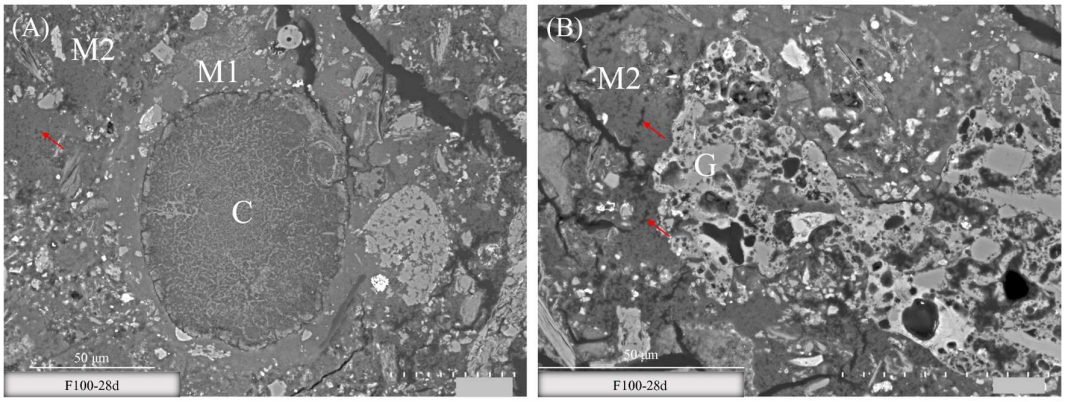

Fig. 7 Comparing SEM microstructural changes of the alkali activated fly ash binder F100 at 28 days around: (A) a calcium-rich nodule labelled C, and (B) a particle from the vitreous phase labelled G; M1 = dense matrix; M2 = porous matrix

Figure 7 shows micrographs of the alkali activated binder after 28 days, and more particularly the difference between microstructural changes occurring (A) around a calcium rich particle identified as the dark reactive zones in optical microscopy, and around a glassy particle identified as the brown matrix in optical microscopy.

It is worth noting that although amorphous and extremely porous the vesicular glassy phases reaction is negligible as its vesicular structure remains similar to the one after 24 hours (see Figure 4A, particle labelled 1). This observation is in accordance with our previous study about the physicochemical evolution of that system which shows that the vitreous phase mainly remains unreactive (Coudert et al., 2019). It is well known that the rate of reaction of the aluminosilicate vitreous phases of fly ash at ambient temperature following alkaline activation is slow and takes several days (Provis and Deventer, 2009; Wardhono et al., 2015). Whereas the calcium-rich particles in our mixes are extremely

and quickly reactive as the formation of new products containing calcium already starts after 24 hours as seen previously in Figure 3. Hence, the faster reaction of calcium-rich particles leads to the formation of dense products (as seen in Figure 7A) freezing the system and preventing the later reaction of the aluminosilicate glassy phases.

Massive and dense areas are observed around calcium-rich nodules (see Figure 7A), while a more porous matrix is seen around vesicular glassy phases (see Figure 7B). The comparison in Figure 7 hence evidences that there are different matrices forming the alkali activated treated soil: (i) a first circularly-shaped matrix identified around calcium-rich particles and presenting a high density labelled M1 on Figure 7A, and (ii) a more porous matrix less bonded labelled M2 on Figure 7A&B whose pores are shown by red arrows, and located around glassy phases of lower reactivity. A previous investigation of that system by Nuclear Magnetic Resonance showed the signature of only one type of silicate chains combined with calcium and spreaded into the matrix as a new compound (Coudert et al., 2019). Therefore, Scanning Electron Microscopy provides an additional information: although the atomic structure of the silicate chain remains similar, the arrangement of those phases in the matrix varies following the local environment. Similarly to the great heterogeneity of fly ash, the matrix formed is also highly heterogeneous.

3.2.3 Mercury Intrusion Porosimetry (MIP)

Figure 8A shows cumulative curves of mercury intrusion porosimetry tests of the alkali activated fly ash binder over time. The longer the curing time, the lower is the cumulative intrusion volume ratio implying a progressive decrease of the overall porosity over time, and in accordance with the general tendencies observed by SEM in section 3.2.2. It is

owed to the progressive filling of pores by the new compounds formed i.e. calcium-silicate two-dimensional chains and thenardite.

Figure 8B shows the frequency distributions of pore entrance diameters belonging to the alkali activated fly ash binder over time. Samples at 24 hours, 3 and 7 days all show one broad modal pore sizes between 0.05 µm and 3 µm. However, from 24 hours to 7 days the frequency of those pores progressively decreases due to their filling by newly formed compounds. Whereas, at 28 days a narrower modal pore size at about 2 µm is observed. By analogy with SEM pictures, those remaining pores at 2 µm could correspond to either the size of the cracks seen around calcium particles and associated with shrinkage as previously observed on Figure 5, the porosity formed within calcium nodules after their dissolution also seen on Figure 5, or else pores that have not been filled by new compounds within the more porous matrix previously identified and labelled M2 on Figure 7.

Finally, in the area of lower pore size i.e. below 20 nm the increase of frequency over time corresponds to the formation of a new class of pores inside the matrix. It is associated with the formation of the silicate two-dimensional chains combined with calcium, whose structure resembles those of Calcium-Silicate Hydrates (i.e. C–S–H phases commonly found in Portland cement) known for possessing an intrinsic porosity of a nanometer size (Muller, 2014). However, this small new class of pores cannot be fully probed by MIP technique whose detection limit in the small entrance pore size is of 7 nm.

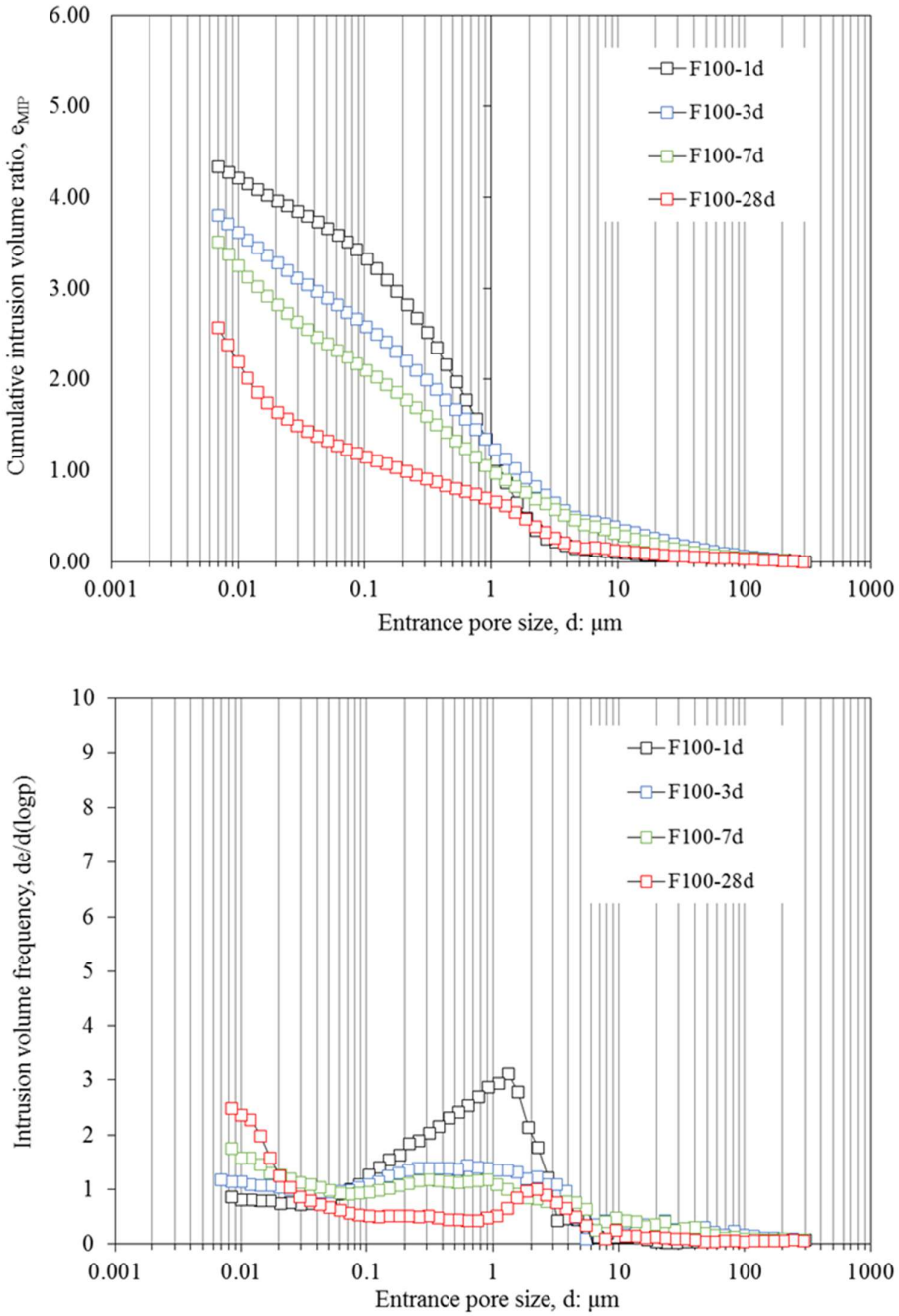

460

461 **Fig. 8** Comparing mercury intrusion porosimeter tests of the alkali activated fly ash binder
462 F100 over time and in terms of (A) cumulative intrusion volume ratios, (B) intrusion
463 volume frequency ratios as a function of entrance pore size.
464

465

466 *3.3 Interaction between the alkali activated fly ash binder and kaolin*

467 The following section aims at understanding the interaction between kaolin and the alkali
468 activated fly ash binder previously described. Our former study focussing on the
469 physicochemical evolution of the same mixes herein studied showed that kaolin was not
470 reactive during alkaline activation and did not modify the reaction sequence when
471 compared to the one of the alkali activated fly ash binder alone (Coudert et al., 2019).
472 Accordingly, similar mechanisms of ions dissolution precipitation from the calcium-rich
473 particles into the matrix leading to the formation of new products also occur in the alkali
474 activated fly ash binder treated soil as previously described for the binder in section 3.2.2,
475 and hence will not be detailed here.
476 Regarding the pore network structure, our previous study also showed that kaolinite
477 platelets were homogeneously spread across the matrix. This section consequently aims
478 at giving a deeper insight of the influence of kaolin on the microstructure with respect to
479 the binder alone.
480 Figure 9 shows microstructural observations of the alkali activated fly ash binder treated
481 soil over time by optical microscopy. Similarly, to the alkali activated fly ash binder, after
482 24 hours of curing, dispersed dark spots corresponding to calcium-rich nodules are seen
483 across the overall sample, whereas at 28 days larger dark zones encompassing the newly
484 formed compounds have grown around those nodules. Hollowed greyish nodule
485 structures at 28 days can also be distinguished as for the binder and associated with the
486 dissolution of calcium-rich particles.
487

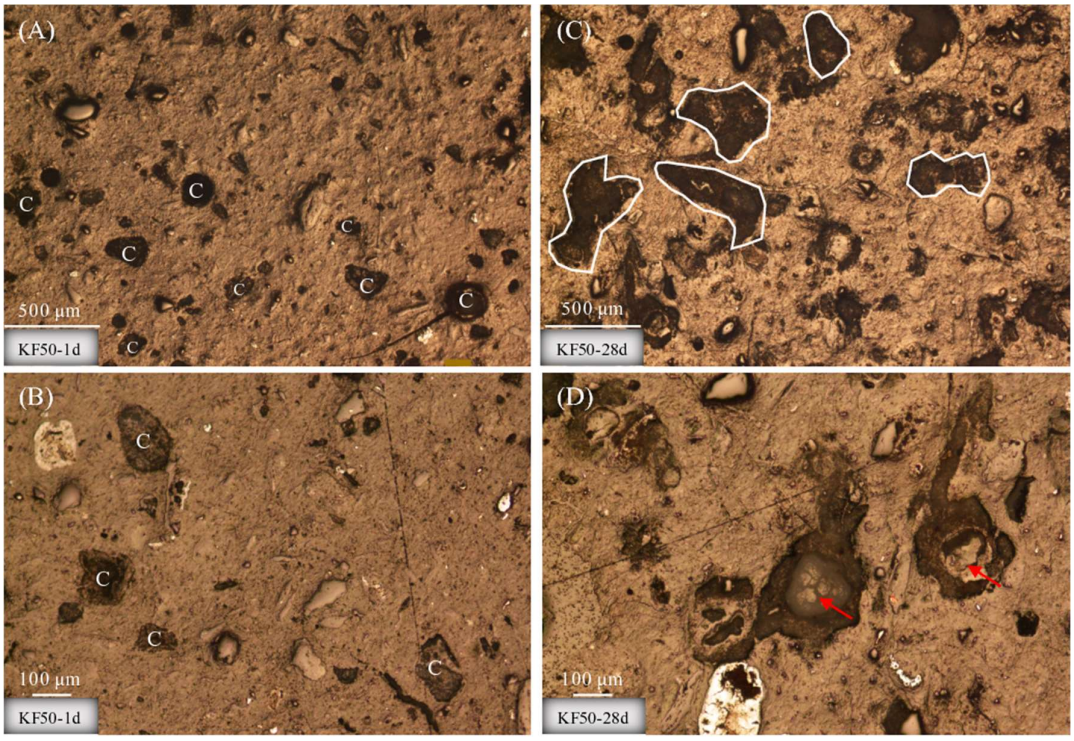

Fig. 9 Optical microscopy images of the alkali activated fly ash binder treated soil KF50 (A) and (B) after 24 hours, (C) and (D) at 28 days, C=calcium-rich particle.

The widening of darker zones which indicates the extent of reaction is lesser than the binder and represents around ¼ of the sample. This is consistent with the proportions of aluminosilicate solid considering that half of fly ash containing the reactive calcium nodules has been replaced by non-reactive kaolin in this soil-binder mixture. Consequently, the growth and development of new products into the available spaces does not seem influenced by the presence of kaolin.

Figure 10 shows micrographs of the alkali activated binder treated soil. After 24 hours crackings around and inside calcium nodules are seen (see particle C on Figure 10A), and associated to shrinkage similarly to the alkali activated fly ash binder at 28 days. The treated soil at 28 days however shows less marked crackings as shown on Figure 10B which focusses on the interface between a calcium-rich nodule labelled 1 and the

surrounding dense matrix labelled 2. It is attributed to the presence of kaolinite acting as a filler at the periphery of the calcium-rich nodules (see red arrows on Figure 10B showing kaolinite platelets).

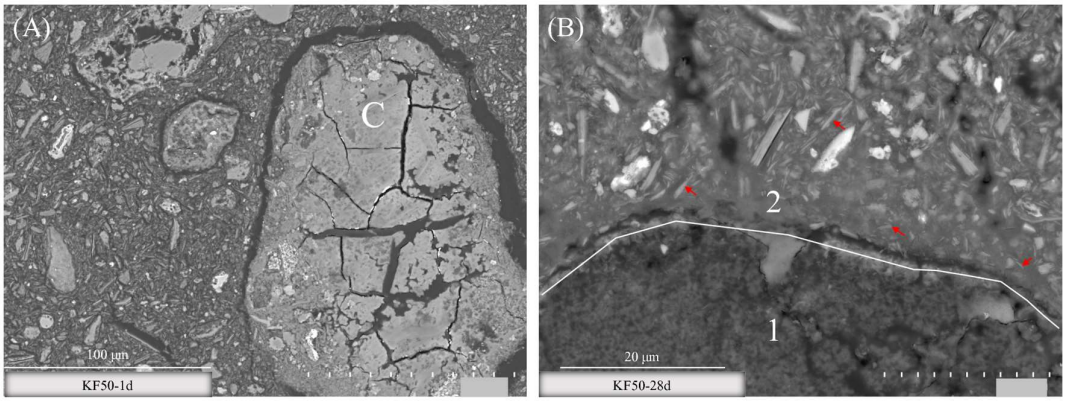

Fig. 10 SEM micrographs of the alkali activated fly ash binder treated soil KF50 at (A) 24 hours and (B) 28 days.

Figure 11A shows cumulative curves of mercury intrusion porosimetry tests of the alkali activated fly ash binder treated kaolin over time. Similarly to what was observed for the alkali activated binder, a decrease of the total porosity is detected over time.

Figure 11B shows the frequency distributions of pore entrance diameters belonging to the treated soil over curing time. Similarly to the alkali activated fly ash binder, the treated soil at 24 hours shows one modal pore sizes. Nevertheless, compared to the binder it is associated with a lower entrance pore size value around 0.4 µm and a much thinner peak. The non-presence of a wide class of pores between 0.05 µm and 3 µm at 24 hours as seen for the alkali activated fly ash binder is associated with the filling of the spaces between the coarse grains of fly ash by the small sized kalinite platelets. At 24 hours, kaolin therefore leads the organisation of the system microstructure as the typical pattern of kaolin (i.e. a monomodal curve with a peak around 0.4 µm) is shaping the curve.

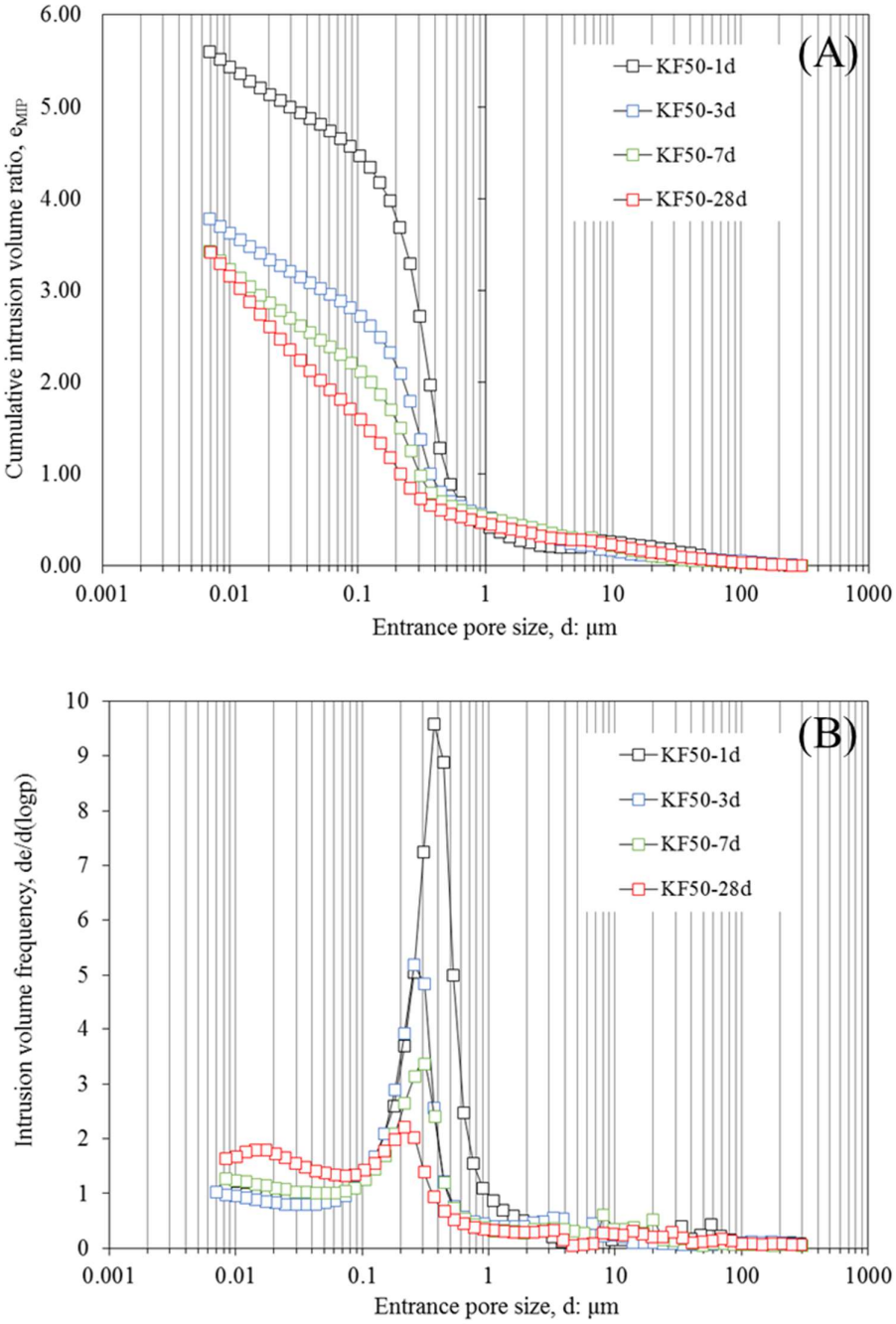

Fig. 11 Comparing mercury intrusion porosimeter tests of the alkali activated fly ash binder treated soil KF50 over time and in terms of (A) cumulative intrusion volume ratios, (B) intrusion volume frequency ratios as a function of entrance pore size.

528 Increasing the curing time, the filling of largest pores around the peak is seen as for the
529 binder and due to the progressive filling of those pores by the newly products formed. A
530 little shift of the residual peak towards smaller entrance diameters is also observed.
531 Finally, the formation of a new class of pores in the area of lower pore size i.e. below 30
532 nm is observed between 7 and 28 days of curing. Similarly to the binder, it is associated
533 with the intrinsic porosity of the newly formed silicate-calcium chains. The delay in
534 detection compared to the binder is due to the lower amount of phases formed for that
535 system.
536 Figure 12 shows the results of one dimensional compression tests on KF20 and KF40
537 treated samples at increasing curing times, namely 24h, 7, 14 and 28 days. Addition of
538 alkali activated binder induces an overall reduction of compressibility of the treated
539 samples, with reduced volume strains for reference vertical stresses. The reduction is
540 more relevant for increasing curing times, showing the stiffer behaviour of the treated
541 sample. Coupled with the reduction of compressibility, an increase of yield stress of the
542 samples is observed. The transition from a reversible behaviour to an irreversible one is
543 shifted (yield stress) to higher vertical stresses. The shift is more relevant for higher
544 amount of binder and at increasing curing time, revealing the reactivity of the binder to
545 promote an improvement of the mechanical response of the treated soil. For stress levels
546 higher than yield stress, treated samples show a higher compressibility coefficient (i.e.
547 slope of the compressibility curve), depending on the destructuration stage induced by
548 load increase, more evident for longer curing times and higher binder content. As a
549 confirmation, in Figure 13 the compressive behaviour of treated samples is reported as
550 function of binder contents. Sample prepared at 10%, 20% and 40% of alkali activated
551 fly ash and cured for 24 hours before testing show a progressive improvement mainly

related to the amount of new compounds forming over time. Compressibility curves show a reduction of compressibility evidenced by the relevant decrease of volume strains and an increase yield stresses of the treated samples, whose extent depends on binder content.

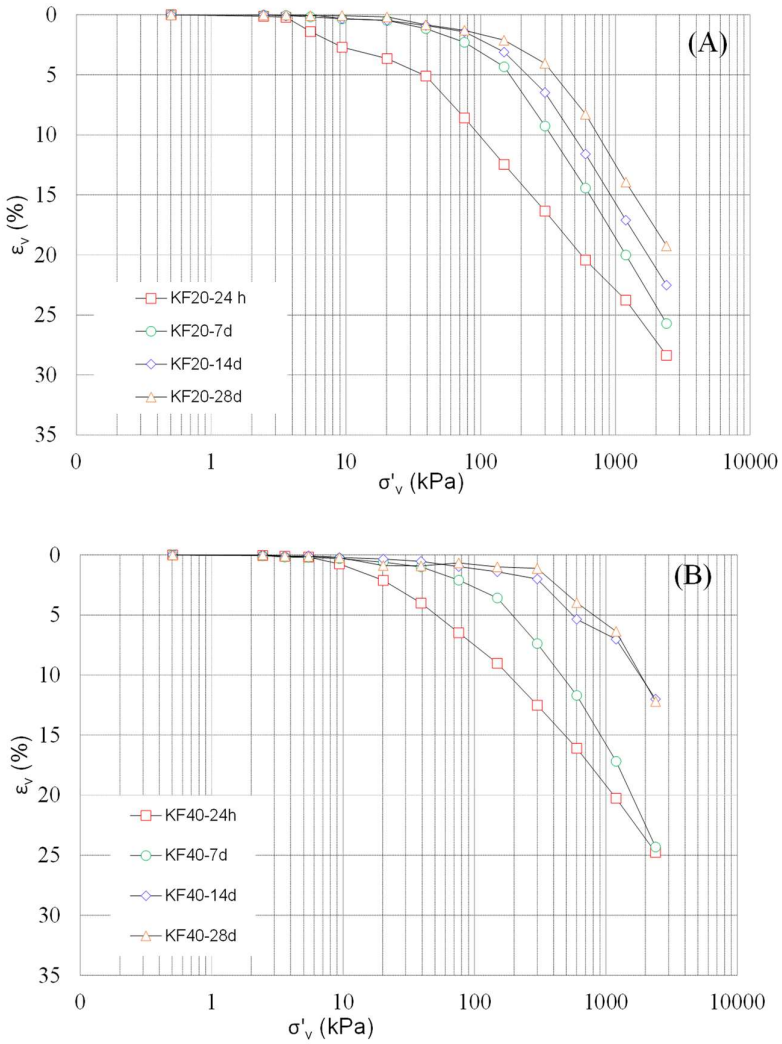

Fig. 12 One dimensional compression curves of alkali activated binder treated samples at 24 h, 7, 14 and 28 days of curing: (A) KF20; (B) KF40.

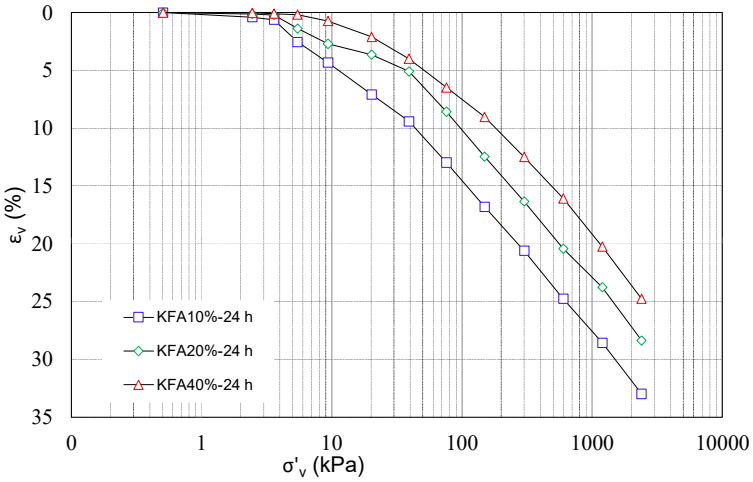

Fig. 13 One dimensional compression curves of treated samples as function of binder contents (i.e. KF10, KF20, KF40) at 24 hours of curing.

3.4 Comparison with Portland cement

This last section focusses on a comparison with microstructural development in Portland cement for which the mechanisms involved appear alike. This comparison particularly helps at providing a better understanding of (i) how microstructures are formed and (ii) interpreting the short and long-term performances of the treated soil regarding the evolution of the binder over time. At macroscopic level, the effectiveness of alkali activated binder soil treatment has been highlighted by comparison with mechanical performance induced by Portland cement.

3.4.1 Processes generating the microstructure

In cement systems, the dissolution of cement particles releases ions into the pore solution which then combine with water to form mainly Calcium Silicate Hydrates C–S–H (Muller, 2014). In a similar way, in our alkali activated binder, the dissolution of calcium-rich particles from fly ash releases calcium cations into the pore solution which then combine with water and silicon anions from the alkaline solution to form silicate two-

579 dimensional chains combined with calcium. A former investigation by Nuclear Magnetic
580 Resonance nevertheless showed that the chains structure is slightly different from C–S–
581 H, namely they are not well organized, of high length and may incorporate aluminum in
582 a three dimensional environment which has not been described in literature yet (Coudert
583 et al., 2019).
584 Secondly, it was reported for cement systems that the first Calcium Silicate Hydrates C–
585 S–H cover cement grains and further grow into the available space. All cement grains are
586 therefore surrounded by a shell of C–S–H (Scrivener, 2004). Again similarly in this study,
587 optical microscopy images clearly show the development and growth of new products
588 around calcium-rich reactive particles suggesting a similar mechanism.
589 Furthermore, Scrivener (2004) shows that as the cement grains dissolve, this might leave
590 a hollow shell (Scrivener, 2004). The various extent of reaction of individual cement
591 grains depends on their sizes: small cement grains hydrate completely in the first stages
592 and remain as hollow shells of hydration product; whereas big grains further hydrate
593 which forms denser hydration products and which fill in the gap between shell and grain
594 (Muller, 2014). In this study it is also noticeable that calcium-rich reactive phases react
595 at different rates: some completely dissolve after 28 days leaving a hollow shell while
596 other remain with their initial structure and still contain calcium. Consequently, and
597 similarly to what is described in the literature, depending on the calcium nodule size, the
598 local products formed slightly differ which could lead to local variation of the inherent
599 material properties.
600
601 *3.4.2 Pore network characteristics*

602 Regarding the pore network characteristics of cement systems, two populations of pores
603 are generally distinguished: (i) capillary pores which correspond to space not being filled
604 by solid products of hydration, and (ii) small pores called gel pores associated to the
605 intrinsic porosity of Calcium Silicate Hydrates C–S–H. Over time, while chemical
606 reactions proceed the population of capillary pores decreases whereas the population of
607 gel pores increases, which may lead to the formation of disconnected spaces (Jennings et
608 al., 2008). Our alkali activated binder shows similar tendencies that is a progressive
609 decrease of intermediate pores or capillary pores while a new class of pores associated
610 with silicate-calcium chain products is detected using Mercury Intrusion Porosimetry.
611

612 *3.4.3 Macroscopic behaviour according to the microstructure evolution*

613 Since both the processes generating the microstructure and the evolution of the pore
614 network over time of our alkali activated binder are similar to cement systems, a similar
615 influence of the microstructure on the short and long-term performances can be expected.
616 Changes in the pore network strongly influence transport properties that govern the rate
617 of all major deterioration processes and the service life of building materials (Wong et
618 al., 2006). Namely the formation of gel pores inside the capillary spaces tends to decrease
619 the connectivity of the pore network inhibiting the transport of aggressive substances such
620 as acids, carbonate or chloride through concrete and therefore enhancing the material
621 durability (van Deventer et al., 2010; Muller, 2014).
622 Finally, despite the great inhomogeneity of the reactive fly ash the growth and widening
623 of new products appear to occur homogeneously across the sample at a millimetric scale
624 in our alkali activated materials which would benefit the formation of a homogeneously
625 reinforced material.

626 At volume scale of the sample, a comparison between the mechanical performance
627 induced by alkali activated binder (KF40) and by ordinary Portland cement (KC40) is
628 shown in Figure 14 for samples prepared with the same binder content and cured for 7,
629 14 and 60 days. No relevant changes in the compressibility curves are observed for KF40
630 and KC40 samples cured for 7 days before testing (Figure 14A). For longer curing times,
631 results show a higher compressibility reduction and yield stress increase for KF40 treated
632 samples compared to cement treated samples (Figures 14B and 14C). The post-yield
633 behaviour induced by ordinary Portland cement shows the highest slope of the
634 compressibility curve, highlighting a more evident destructuration stage for cement
635 treated samples at increasing vertical stresses.

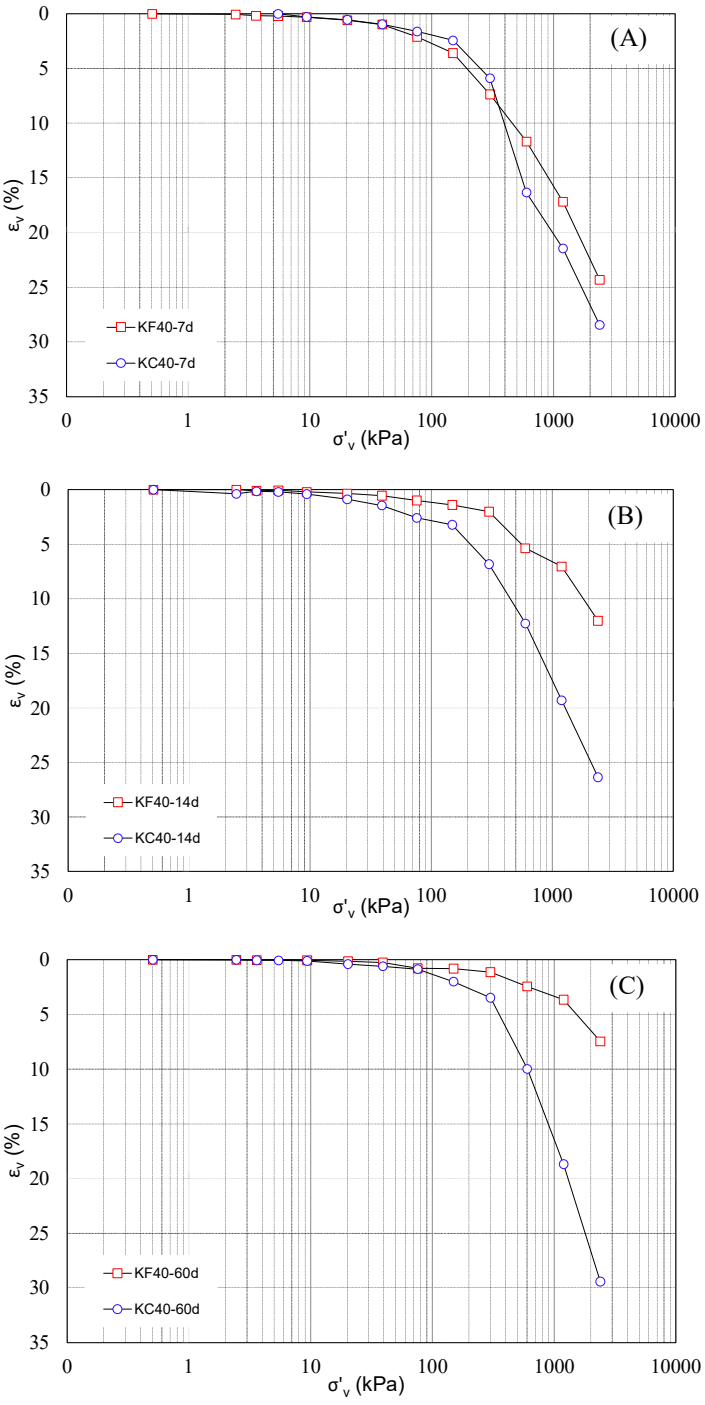

636

637 **Fig. 14** One dimensional compression curves of treated samples as function of binder
638 type (i.e. KF40 vs. KC40): (A) 7 days of curing; (B) 14 days of curing; (C) 60 days of
639 curing
640

641

3 Conclusions

The development of a novel binder that is an alkali activated calcium-rich fly ash for clay soil stabilisation was investigated. The study of its microstructural evolution showed that structural changes occur around calcium-bearing minerals from fly ash which constitute the reactive phases, and whose dissolution leads to the formation of new compounds on its surface first and then growing into the available space. Capillary pore spaces are progressively filled by new compounds (i.e thernadite and silicate-calcium chains) over time. Whereas the newly formed silicate-calcium chains possess an intrinsic porosity of nanometric size conducting to the formation of a new class of small pores over time. Different heterogenous matrices of various porosity and arrangement are however observed across the material and owed to the high heterogeneity of fly ash whose particles locally react differently.

The interaction between the binder and kaolin showed that small sized kaolinite platelets fill the spaces between coarser grains from fly ash. Kaolin is therefore leading the microstructural organisation, that is, the pore network is characterised by pores ranging in lower size compared to the binder. Nevertheless, the microstructural changes remain similar over time i.e. filing of capillary pores and appearance of nanometric pores from silicate-calcium chains.

One-dimensional compression tests performed on treated sample highlighted the effectiveness of alkali activated binders to promote an improvement of the mechanical behaviour of treated soil. A reduction of compressibility and increase of the yield stress soil was observed since the very short term.

The observed microstructural evolution is similar to the one of cement system and should therefore conducts to akin performances that is an increase in strength and ability to resist

to aggressive substances due to changes in transport properties. It has been confirmed by observing the similarities of the mechanical performance of alkali activated binder treated samples with cement treated ones for short curing time. A marked improvement of the mechanical behaviour of soil is induced by alkali activated binder starting from 14 days of curing, representing a viable sustainable alternative to the use of ordinary stabilizing agent for soil improvement.

However, regarding the complexity of both cement and alkali activated systems which are multi-components systems, a coupling of those microstructural observations with mechanical performances and transport properties is of further interest. Namely, a complementary three-dimensional characterisation of the pore network using for instance microtomography would greatly help to assess the connectivity and tortuosity of the pore network which are primordial parameters to understand properly transport properties and therefore durability. Using micro-indentation coupled with Scanning Electron Imaging would also allow to measure local hardness variations following the extent of reaction of calcium particles and therefore help to apprehend how significant are the local microstructural variations for the mechanical performances at a macroscopic scale.

Acknowledgements

The authors wish to acknowledge the support of the European Commission via the Marie Skłodowska-Curie Innovative Training Networks (ITN-ETN) project TERRE 'Training Engineers and Researchers to Rethink geotechnical Engineering for a low carbon future' (H2020-MSCA-ITN-2015-675762).

References

690 Askeland, D.R., Fulay, P.P., Wright, W.J., 2011. The science and engineering of
691 materials, 6th ed. ed. Cengage Learning, Stamford, CT.
692 Basha E.A., Hashim R., Muntohar A., 2003. Effect of the cement-rice husk ash on the
693 plasticity and compaction of soil, Electron. J. Geotech. Eng. 8.
694 Buchwald, A., Kaps, C., Hohmann, M., 2003. Alkali-activated binders and pozzolan
695 cement binders–complete binder reaction or two sides of the same story, in: Proceedings
696 of the 11th International Conference on the Chemistry of Cement. Portland Cement
697 Association Durban, South Africa, pp. 1238–1246.
698 Chemeda, Y., 2015. Effect of hydrated lime on kaolinite surface properties and its
699 rheological behaviour. Université de Nantes.
700 Clemens, H., Mayer, S., Scheu, C., 2008. Microstructure and Properties of Engineering
701 Materials. Neutrons Synchrotron Radiat. Eng. Mater. Sci. Fundam. Appl. 1–20.
702 Coudert, E., Paris, M., Deneele, D., Russo, G., Tarantino, A., 2019. Use of alkali activated
703 fly ash binder for kaolin clay soil stabilisation: Physicochemical evolution. Constr. Build.
704 Mater. 201 (2019) 539–552, https://doi.org/10.1016/j.conbuildmat.2018.12.188
705 Cristelo, N., Glendinning, S., Fernandes, L., Pinto, A.T., 2012. Effect of calcium content
706 on soil stabilisation with alkaline activation. Constr. Build. Mater. 29, 167–174.
707 https://doi.org/10.1016/j.conbuildmat.2011.10.049
708 Cristelo, N., Glendinning, S., Teixeira Pinto, A., 2011. Deep soft soil improvement by
709 alkaline activation. Proc. Inst. Civ. Eng. - Ground Improv. 164, 73–82.
710 https://doi.org/10.1680/grim.900032
711 Duxson P, Provis JL, Lukey GC, Van Deventer JS, 2007. The role of inorganic polymer
712 technology in the development of ‘green concrete’. Cem. Concr. Res. 2007; 37:1590–7
713 Fang, G., Bahrami, H., Zhang, M., 2018. Mechanisms of autogenous shrinkage of alkali-

714 activated fly ash-slag pastes cured at ambient temperature within 24 h. Constr. Build.
715 Mater. 171, 377–387. https://doi.org/10.1016/j.conbuildmat.2018.03.155
716 James J., Pandian P.K., 2016. Industrial wastes as auxiliary additives to cement/lime
717 stabilization of soils, Adv. Civ. Eng. 2016 1–17.
718 Jennings, H.M., Bullard, J.W., Thomas, J.J., Andrade, J.E., Chen, J.J., Scherer, G.W.,
719 2008. Characterization and Modeling of Pores and Surfaces in Cement Paste:
720 Correlations to Processing and Properties. J. Adv. Concr. Technol. 6, 5–29.
721 Lawrence, M., Jiang, Y., 2017. Porosity, Pore Size Distribution, Micro-structure, in:
722 Amziane, S., Collet, F. (Eds.), Bio-Aggregates Based Building Materials. Springer
723 Netherlands, Dordrecht, pp. 39–71. https://doi.org/10.1007/978-94-024-1031-0_2
724 McLellan BC, Williams RP, Lay J, Van Riessen A, Corder GD., 2011. Costs and carbon
725 emissions for geopolymer pastes in comparison to Ordinary Portland Cement. J. Clean
726 Prod 2011; 19:1080–90
727 Muller, A.C.A., 2014. Characterization of porosity & CSH in cement pastes by 1H NMR.
728 École Polytechnique Fédérale de Lausanne, Suisse.
729 Nalbantoğlu Z., 2004. Effectiveness of class C fly ash as an expansive soil stabilizer,
730 Constr. Build. Mater. 18, 377–381.
731 Nath, S.K., Maitra, S., Mukherjee, S., Kumar, S., 2016. Microstructural and
732 morphological evolution of fly ash based geopolymers. Constr. Build. Mater. 111, 758–
733 765. https://doi.org/10.1016/j.conbuildmat.2016.02.106
734 Provis, J.L., Deventer, J.S.J. va., 2009. Geopolymers Structure, processing, properties
735 and industrial applications, Woodhead Publishing in materials. Woodhead, Cambridge.
736 Rios, S., Cristelo, N., Viana da Fonseca, A., Ferreira, C., 2016. Structural Performance
737 of Alkali-Activated Soil Ash versus Soil Cement. J. Mater. Civ. Eng. 28, 4015125.

738 https://doi.org/10.1061/(ASCE)MT.1943-5533.0001398
739 Sargent, P., 2015. The development of alkali-activated mixtures for soil stabilisation. In
740 Handbook of alkali-activated cements, mortars and concretes (pp. 555-604). Woodhead
741 Publishing
742 Scrivener, K.L., 2004. Backscattered electron imaging of cementitious microstructures:
743 understanding and quantification. Cem. Concr. Compos. 26 8 935–945.
744 Scrivener, K.L., Kirkpatrick, R.J., 2008. Innovation in use and research on cementitious
745 material. Cem. Concr. Res. 38, 128–136.
746 https://doi.org/10.1016/j.cemconres.2007.09.025
747 Shi, C., Krivenko, P.V., Roy, D.M., 2006. Alkali-activated cements and concretes. Taylor
748 & Francis, London ; New York.
749 Silva, R.A., Oliveira, D.V., Miranda, T., Cristelo, N., Escobar, M.C., Soares, E., 2013.
750 Rammed earth construction with granitic residual soils: The case study of northern
751 Portugal. Constr. Build. Mater. 47, 181–191.
752 https://doi.org/10.1016/j.conbuildmat.2013.05.047
753 Singhi, B., Laskar, A.I., Ahmed, M.A., 2016. Investigation on Soil–Geopolymer with
754 Slag, Fly Ash and Their Blending. Arab. J. Sci. Eng. 41, 393–400.
755 https://doi.org/10.1007/s13369-015-1677-y
756 Tenn, N., Allou, F., Petit, C., Absi, J., Rossignol, S., 2015. Formulation of new materials
757 based on geopolymer binders and different road aggregates. Ceram. Int. 41, 5812–5820.
758 https://doi.org/10.1016/j.ceramint.2015.01.010
759 United Nations, 2004. A More Secure World: Our Shared Responsibility. Report of the
760 Secretary-General's High-level Panel on Threats, Challenges and Change, 2004.
761 van Deventer, J.S.J., Provis, J.L., Duxson, P., Brice, D.G., 2010. Chemical Research and

762 Climate Change as Drivers in the Commercial Adoption of Alkali Activated Materials.
763 Waste Biomass Valorization 1, 145–155. https://doi.org/10.1007/s12649-010-9015-9
764 van Deventer, J.S.J., San Nicolas, R., Ismail, I., Bernal, S.A., Brice, D.G., Provis, J.L.,
765 2015. Microstructure and durability of alkali-activated materials as key parameters for
766 standardization. J. Sustain. Cem.-Based Mater. 4, 116–128.
767 https://doi.org/10.1080/21650373.2014.979265
768 Vitale E., Russo G., Deneele D. 2019. Multi-scale analysis on soil improved by alkali
769 activated binders. E3S Web of Conferences 92, 11003 (2019) - IS-Glasgow 2019;
770 https://doi.org/10.1051/e3sconf/20199211003
771 Vitale E., Marocco A., Khatib M., Russo G. 2020a. Hydro-mechanical behaviour of
772 alkali-activated binder treated soil. E3S Web of Conferences 195, 06003 (2020) – E-
773 UNSAT 2020; https://doi.org/10.1051/e3sconf/202019506003
774 Vitale E., Russo G., Deneele D. 2020b. Use of Alkali-Activated Fly Ashes for Soil
775 Treatment. Geotechnical Research for Land Protection and Development. CNRIG 2019.
776 Lecture Notes in Civil Engineering, vol 40. Springer
777 Vitale, E., Russo, G., Dell'Agli, G., Ferone, C., and Bartolomeo, C. 2017. Mechanical
778 behaviour of soil improved by alkali activated binders. Environments 4(4), 80.
779 https://doi.org/10.3390/environments4040080
780 Wardhono, A., Law, D.W., Strano, A., 2015. The Strength of Alkali-activated Slag/fly
781 Ash Mortar Blends at Ambient Temperature. Procedia Eng. 125, 650–656.
782 https://doi.org/10.1016/j.proeng.2015.11.095
783 Wilkinson, A., Haque, A., Kodikara, J., 2010. Stabilisation of clayey soils with industrial
784 by-products: part A. Proc. Inst. Civ. Eng. - Ground Improv. 163, 149–163.
785 https://doi.org/10.1680/grim.2010.163.3.149

786 Wong, H.S., Buenfeld, N.R., Head, M.K., 2006. Estimating transport properties of
787 mortars using image analysis on backscattered electron images. Cem. Concr. Res. 36,
788 1556–1566.
789 Xi F., Davis S. J., Ciais P., Crawford-Brown D., Guan D., Pade C., Shi T., Syddall M.,
790 Lv J., Ji L., Bing L., Wang J., Wei W., Yang K.-H., Lagerblad B., Galan I., Andrade C.,
791 ZhangY., Liu Z. 2016. Substantial global carbon uptake by cement carbonation, Nature
792 Geoscience, 9, 12-2016
793 Zhang Z, Provis JL, Reid A, Wang H., 2014. Geopolymer foam concrete: an emerging
794 material for sustainable construction. Constr Build Mater 2014; 56:113–27.
795 Zhang, M., Guo, H., El-Korchi, T., Zhang, G., Tao, M., 2013. Experimental feasibility
796 study of geopolymer as the next-generation soil stabilizer. Constr. Build. Mater. 47,
797 1468–1478. https://doi.org/10.1016/j.conbuildmat.2013.06.017
798